

Article

Influence of Damping Plate Size on Pitch Motion Response of Floating Offshore Wind Turbine

Jie Xu ¹, Chuansheng Wang ², Jiawen Li ³, Yichen Jiang ^{2,*}, Guangyin Tang ^{4,*} and Yi Yang ⁵

¹ Guangdong Datang International Chaozhou Power Generation Co., Ltd., Chaozhou 515700, China; dtczdc@163.com

² School of Naval Architecture, Dalian University of Technology, Dalian 116024, China; wcoyox@outlook.com

³ Navigation College, Dalian Maritime University, Dalian 116026, China; lijiawen@dlmu.edu.cn

⁴ Offshore Technology Center of CCS, Tianjin 300457, China

⁵ China Southern Power Grid Electric Power Technology Co., Ltd., Guangzhou 510020, China; yyxt007@sina.cn

* Correspondence: ycjiang@dlut.edu.cn (Y.J.); gy.tang@hotmail.com (G.T.)

Abstract: For floating offshore wind turbines, a significant pitch and roll motion response of the platform can affect the acceleration and power generation of the nacelle. The damping plate is considered a type of attachment that can be used to reduce rotational motion, but research on its anti-rotational effect is limited. The objective of this work is to analyze the impact of installing damping plates and varying their sizes on the pitch motion response of semi-submersible platforms, while also proposing optimization strategies for damping plate design. Firstly, a comparison between numerical simulations and experimental measurements validates the accuracy of the CFD calculations. Subsequently, different sizes of damping plates are proposed for the platforms, followed by simulations under various conditions. Finally, comprehensive data analysis is conducted. The findings suggest that installing damping plates enhances both the platform's added moment of inertia and damping coefficients while simultaneously amplifying its motion response in regular waves. Furthermore, increasing the size of damping plates leads to an increase in both the added moment of inertia and motion response for the platform, whereas the damping coefficient exhibits an initial increasing trend followed by a subsequent decrease. Ultimately, it is found that increasing the distance between damping plates and the free surface significantly reduces wave-induced loads on the platform.

Keywords: damping plate; size; semi-submersible platform; pitch motion response



Citation: Xu, J.; Wang, C.; Li, J.; Jiang, Y.; Tang, G.; Yang, Y. Influence of Damping Plate Size on Pitch Motion Response of Floating Offshore Wind Turbine. *J. Mar. Sci. Eng.* **2024**, *12*, 1600. <https://doi.org/10.3390/jmse12091600>

Academic Editor: Spyros A. Mavrakos

Received: 26 July 2024

Revised: 20 August 2024

Accepted: 4 September 2024

Published: 10 September 2024



Copyright: © 2024 by the authors. Licensee MDPI, Basel, Switzerland. This article is an open access article distributed under the terms and conditions of the Creative Commons Attribution (CC BY) license (<https://creativecommons.org/licenses/by/4.0/>).

1. Introduction

Floating offshore wind turbine (FOWT) offers a promising solution for harnessing electric power from renewable energy sources. However, with the increasing size of wind turbines, the motion response of floating foundations becomes more significant, resulting in considerable acceleration of the turbine nacelle even at small inclinations and significantly impacting normal turbine operation. Additionally, due to the existence of rotor and tower, the FOWT is subjected to a greater wind heeling moment than the conventional floating platform, which would cause significant pitch motion and bring great challenges to the structural safety and power generating efficiency [1]. Therefore, further efforts are required to mitigate platform's pitch motion response and ensure stable turbine operation.

The foundations of offshore wind turbines present one of the main challenges in offshore wind turbine design [2], which has three main FOWT concepts: semi-submersible, spar, and tension leg platform. Although there are other ways, such as an isolated deck for large floating systems, which are also seen as successful alternates to support wind turbines [3,4], the semi-submersible one is receiving significant attention due to several advantages: these types of platforms can be fully assembled onshore and towed ready-to-use to their final destinations; the available mooring systems are well known and

cost-competitive; if properly designed, the downtime in operational sea states due to excessive platform motion is low [5]. Koo et al. [6] performed a model test project called OC4 (Offshore Code Comparison Collaboration Continuation) at MARIN (Maritime Research Institute Netherlands). The test data were used for the calibration and improvement of the existing design analysis and performance numerical codes, which significantly supported subsequent research by other scholars. Goupee et al. [7] compared the hydrodynamic performance of three distinct platforms (tension leg platform, spar-buoy, and semisubmersible) using the model test data and demonstrated the unique advantages and disadvantages of each. Coulling et al. [8] used publicly available MARIN data, calibrated the FAST model, and performed a series of studies. The results showed that FAST performed well in predicting the coupled aero-hydro-elastic response of the DeepCwind semi-submersible floating wind turbine. Li et al. [9,10] replaced the original viscous damping model implemented in FAST with a quadratic one to gain an accurate capture of viscous effects and investigated the joint wind-wave induced dynamic responses of a semi-type offshore floating wind turbine under normal states and fault event conditions, along with the wave-wind induced global motion and mooring system responses. Due to the dissimilar scaling issues, the conventional experimental method of FOWT can hardly be used directly to validate the full-scale global dynamic responses accurately [11]. Chen et al. [12] provided a detailed introduction to the development status, characteristics, and limitations of the accurate simulation methods of the aerodynamic loads under the Froude scaling law, along with their comparisons. Li et al. [13,14] focused on the DeepCwind semi-submersible platform and NREL's 5 MW reference turbine and conducted studies via model test. An improved method was proposed to correct the deficient thrust force in a Froude scale experimental condition, which was able to simulate the rotor operational state more realistically by allowing the rotor to rotate freely with the wind, and they developed a MATLAB code simulating the global motion responses of offshore floating wind turbines. The results showed that the dynamic response of the mooring line is mainly dominated by wave loads and the aerodynamic effect can be simplified as an extra constant force. Wang et al. [15] conducted hydrodynamic studies on the heave motion of the DeepCwind semi-submersible platform using the CFD method. Their results indicated that significant changes in the vorticity and hydrodynamic pressure are mostly found around the damping plates and the presence of damping plates largely influences the hydrodynamic damping. Zong et al. [16] studied the short-term motion responses of FOWT under extreme wind-wave excitation based on STAR-CCM+ and FAST and compared results under the same wind and wave sea state between STAR-CCM+ and FAST. The comparison revealed good agreement in predicting heave and pitch motion responses but found significant differences in other motion responses and mooring tensions. Chen et al. [17] combined a DeepCwind semi-submersible FOWT and a point absorber wave energy convertor (PAWEC) to form a novel integrated floating wind-wave generation platform (FWWP). The study found that the existence of the PAWEC generally has no effect on the wind power generation of the FWWP, but it may help to reduce the heave motion of the platform of the FWWP to some extent due to the coupling effects of the PTO system between the PAWEC and FOWT.

To mitigate the motion response of FOWT, numerous scholars have embarked on research for design optimization, including the utilization of distinct mooring layouts [18,19] and damping plates, among which the attachment of a damping plate at the bottom of the floating structure has been suggested as an effective tool to control its heave motion. Zhang et al. [20] used the forced oscillation method to conduct experimental investigations of the hydrodynamic performance of the damping plates, and studied the impacts of the KC number, oscillation frequency, diameter ratio, and thickness ratio of the damping plate on the added mass and damping coefficients. The results show that the added mass and damping coefficients are independent of oscillation frequencies, while the KC number significantly influences the hydrodynamic coefficients. At the same time, increasing the diameter ratios will decrease the added mass and damping coefficients, and the thinner damping plates obtain larger damping coefficients. Tao et al. [21] conducted model scale

forced oscillation experiments, studied the hydrodynamic characteristics of oscillatory solid or porous disks, along with the sensitivity of damping, and added mass coefficients to both motion amplitude and the disk porosity. An et al. [22] performed experiments and numerical studies on the forced harmonic heave motion of horizontally submerged and perforated rectangular plates, exploring the effects of the perforation ratio, plate submergence, forcing period, and heave amplitude on added mass and damping. Lopez-Pavon et al. [5] conducted forced heave oscillation tests for a range of frequencies and amplitudes and investigated the influence of the vertical flap at the edge of a semi-submersible FOWT's damping plates on the hydrodynamic coefficients through a results comparison with the solid plain model. Zhu et al. [23] conducted a wave flume experiment, which was performed with a scaled floating model; the motion responses of a scaled model in a water flume (i.e., forced oscillation, free decay, and regular wave response) were analyzed. The results indicated that varying the damping plate diameter had the most significant effect on the added mass compared to the gap and KC number (0.2–1.4).

Given the significant advancements in heave performance of platforms equipped with damping plates, previous studies have extensively investigated their impact. However, limited research has been conducted on the influence of damping plates on pitch performance. This study employs a CFD approach based on Reynolds-Averaged Navier–Stokes (RANS) equations coupled with a Volume of Fluid (VOF) multiphase flow model to investigate the DeepCwind semi-submersible platform's forced pitch motions in calm water and 1-DOF pitch motions in regular waves through numerical simulations. The primary focus is to examine how damping plates and their sizes affect the platform's pitch motion response.

2. Numerical Calculation Method

2.1. Numerical Calculation Procedure

The procedure begins with the construction of a numerical wave tank, followed by fine-tuning the wave height of regular waves to achieve the desired level of error accuracy. Subsequently, the DeepCwind semi-submersible platform is introduced to compute its pitch free decay motion in calm water, ensuring computational accuracy through comparison with model test data. Finally, simulations are conducted to analyze various responses of platform pitch motion, and the resulting data are analyzed. The flowchart illustrating the numerical computation process is presented in Figure 1. The main nomenclature definitions used in this paper are shown in Table 1.

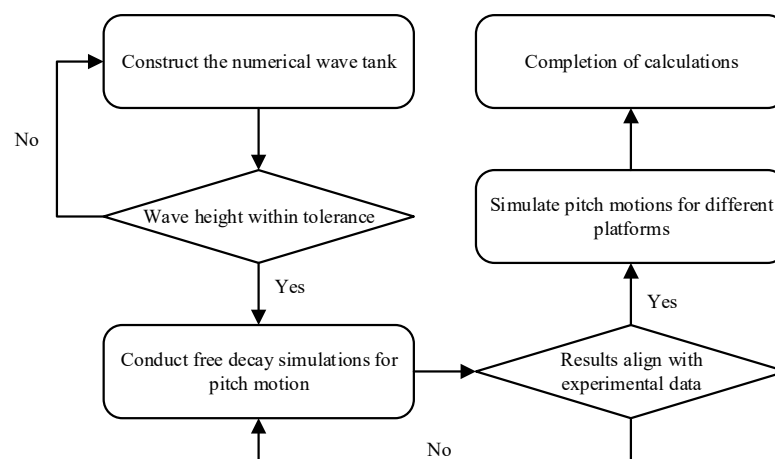


Figure 1. Numerical calculation flowchart.

Table 1. Definition of the main nomenclature.

Symbols	Definition
L_h	Increased distance along the radius of the offset column
H	Wave height
θ_{55}	Pitch angle
M_{55}	Pitch moment
A_{55}	Added moment of inertia
A_{55}^*	Non-Dimensional added moment of inertia
A_{p55}^*	Non-Dimensional added moment of inertia for platform
A_{h55}^*	Non-Dimensional added moment of inertia for heave plate
B_{55}	Damping coefficient
B_{55}^*	Non-Dimensional damping coefficient
B_{p55}^*	Non-Dimensional damping coefficient for platform
B_{h55}^*	Non-Dimensional damping coefficient for heave plate

2.2. Mathematical Model

2.2.1. Viscous Fluid Control Equations

The computations are conducted using viscous fluids, and the governing equations for the viscous flow field primarily comprise the continuity equation and the momentum conservation equation:

$$\frac{\partial \rho}{\partial t} + \nabla \cdot (\rho \mathbf{V}) = 0 \tag{1}$$

$$\rho = \frac{D\mathbf{V}}{Dt} \rho f - \nabla p + \mu \nabla^2 \mathbf{V} \tag{2}$$

where ρ is fluid density, \mathbf{V} is velocity vector, f is unit mass force, p is fluid pressure, and μ is fluid dynamic viscosity coefficient.

In this paper, the finite volume method and RANS turbulence model are employed to analyze the viscous fluids.

2.2.2. First-Order VOF Wave Model

In numerical simulations involving two-phase flow concerning wave-related issues, accurately capturing the free surface is crucial. In STAR-CCM+, the VOF wave model is employed to simulate surface gravity waves at the interface between light and heavy fluids. This model accurately captures strongly nonlinear and intricate free surfaces, offering fast computation speeds and yielding simulation results close to reality. Therefore, it is widely used in numerical simulations involving the interaction between marine structures and waves.

In addition to the continuity equation and the momentum conservation equation, the governing equation of the VOF method also satisfies the following phase equation of the VOF model:

$$\frac{\partial C}{\partial t} + \vec{\mathbf{U}} \cdot \nabla C = 0 \tag{3}$$

where C is phase volume function, representing the proportion of water in the control unit and $\vec{\mathbf{U}}$ is velocity field.

The VOF wave model utilizes a first-order approximation of Stokes wave theory to model first-order waves. This approximation generates waves with a regular sinusoidal distribution. The equation for wave height is represented as

$$\eta = a \cos(\mathbf{K} \cdot \mathbf{x} - \omega t) \tag{4}$$

where a is wave amplitude, \mathbf{K} is wave vector, and ω is wave frequency.

Once the water depth and wave period are determined, the wave length can be calculated based on the dispersion relationship, expressed as

$$\left(\frac{2\pi}{T}\right)^2 = g \frac{2\pi}{L} \tanh\left(\frac{2\pi}{L}d\right) \tag{5}$$

where T is the wave period, g is gravitational acceleration (taken as 9.81 m/s^2), L is wave length, and d is water depth.

In this paper, a first-order VOF wave is used as the input wave to simulate the platform’s 1-DOF pitch motion in regular waves, this is a preliminary investigation assessing the proof of concept. In the future, we will conduct the further investigation for the irregular incident waves.

2.2.3. Wave Force Mitigation Method

In many applications of VOF waves, there is a need for long-duration transient fluid simulations around bodies. Although fluids often generate within larger domains, the focus is typically on solving in the immediate vicinity of the body. STAR-CCM+ integrates three-dimensional fluid simulations with theoretical solutions specified by VOF waves. Within a certain distance around the body, it enforces the solution of the three-dimensional Navier–Stokes equations to converge towards the simplified theoretical solution. This approach reduces the computational domain, lessening computational workloads while maintaining precision and reliability of the solution.

The VOF wave model in STAR-CCM+ encompasses wave forces and wave damping functionalities. This paper employs the wave force functionality, which not only reduces computational loads but also eliminates issues related to surface wave reflection at boundaries caused by progressive force-induced damping. This helps avoid interference from boundary reflections.

The wave force is applied only to momentum without adding phase sources or turbulent sources. It is obtained by adding a source term to the momentum equation in the following form:

$$q_\phi = -\gamma\rho(\phi - \phi^*) \tag{6}$$

where γ is force coefficient, ρ is fluid density, ϕ is current solution of the momentum equation, and ϕ^* is value approached by the force solution.

2.2.4. Wave Height Correction Method

In numerical tank simulations of three-dimensional regular waves based on viscous flow theory, wave attenuation often occurs due to numerical dissipation or insufficiently refined grid partitioning. Hence, it becomes necessary to analyze and rectify the attenuation of regular waves to achieve the desired wave generation effect. The specific method for correcting wave amplitude is as follows:

Assuming the theoretical wave height is H_0 , the wave height before correction is H_1 . The attenuation amount Δ is calculated as

$$\Delta = (H_0 - H_1)/H_0 \tag{7}$$

The corrected wave height H_2 is then calculated as

$$H_2 = (1 + \Delta)H_0 \tag{8}$$

In addition, the viscous flow model is verified in Section 3, and the formula for calculating the relative error δ is similar to Equation (7), which is expressed as follows:

$$\delta = (X - Y)/Y \times 100\% \tag{9}$$

where Y is the standard value, which is the value corresponding to the minimum time step, the maximum number of grids or the model test and X is the comparison value, except for Y .

2.3. Data Processing Method

2.3.1. Viscous Damping Moment Coefficients Calculation Method

As floating platforms under the action of regular waves tend to exhibit forced motion with a nearly constant amplitude, hydrodynamic coefficients can be derived based on the method for forced motion. The following elucidates the calculation method for determining the coefficient of viscous damping moment. Taking the pitch motion as an example, given the platform's motion as follows:

$$\theta_{55} = \theta_0 \sin(\omega t) \tag{10}$$

where θ_{55} is pitch angle, θ_0 is pitch angle amplitude, and ω is pitch motion frequency.

Based on the pitch moment of the platform obtained from CFD calculations, the mathematical expression for the platform's moment can be organized as

$$M_{55} = M_{55,\mu} \sin(\omega t) + M_{55,\lambda} \cos(\omega t) \tag{11}$$

where M_{55} is the pitch moment (relative to the platform's center of gravity) exerted on the platform's pitch motion and $M_{55,\mu}$ and $M_{55,\lambda}$ are constant coefficients, which can be determined by fitting using the `lsqcurvefit` function provided in MATLAB R2020b.

Derived from the free motion equation

$$A_{55}\ddot{\theta}_{55} + B_{55}\dot{\theta}_{55} + M_{55} = 0 \tag{12}$$

where A_{55} is added moment of inertia and B_{55} is damping coefficient.

Substituting Equations (10) and (11) into Equation (12), the added moment of inertia is obtained as

$$A_{55} = \frac{M_{55,\mu}}{\theta_0 \omega^2} \tag{13}$$

The damping coefficient is calculated as

$$B_{55} = -\frac{M_{55,\lambda}}{\theta_0 \omega} \tag{14}$$

In this paper, data from the stable segment of the pitch motion is selected first. Then, half of the mean difference between peak and valley values of the five periods is calculated to determine the pitch motion amplitude θ_0 . Finally, using the above formulas, different platforms' corresponding added moment of inertia and damping coefficients are obtained.

2.3.2. Hydrodynamic Coefficients Non-Dimensionalization Method

After obtaining the added moment of inertia and damping coefficients, it is necessary to non-dimensionalize them. Referring to the formula defined in Wilson et al.'s paper [24], the non-dimensional added moment of inertia is calculated as

$$A_{55}^* = \frac{A_{55}}{m \cdot R^2} \tag{15}$$

where m is the platform mass without damping plates and R is the platform's circumscribed circle radius, which is 0.81735 m.

The non-dimensional damping coefficient is given by

$$B_{55}^* = -\frac{B_{55}}{m \cdot R^2} \sqrt{\frac{R}{2g}} \tag{16}$$

3. Simulation Model

3.1. Numerical Wave Tank Model

In order to accurately simulate the motion response of a FOWT platform in waves, it is necessary to first simulate waves that meet the requirements, so as to obtain the interaction between waves and the floating platform and calculate as accurately as possible the loads exerted by waves on the floating platform. In this section, a three-dimensional numerical wave tank model is established using CFD software STAR-CCM+ 2020.1, conducting numerical simulation and correction of regular waves and obtaining a numerical water tank that can simulate ideal wave heights, thereby laying a solid foundation for subsequent numerical simulations of FOWT platforms in wave conditions.

Li et al. conducted a large-scale model test program of the DeepCwind semi-submersible platform in the Deepwater Offshore Basin at Shanghai Jiao Tong University. The Froude scale method was applied during the model test, which was carried out at a Froude scale of 1:50. Referring to the wave parameters used in Li et al.'s paper [14] and scaling them down by a factor of 1:50, a first-order VOF wave with a height of 0.12 m and a period of 1.414 s was selected as the input. Calculations based on dispersion relationship yielded a wave length of 3.12168 m for this wave.

Once the wave parameters are determined, the construction of the numerical wave tank begins. Initially, the dimensions of the numerical tank are determined based on the selected regular waves, as illustrated in Figure 2. The water depth is consistent with that provided in Li et al.'s paper [14], and the coordinate origin position is set at the center of the calm water surface. To mitigate strong wave reflections at the end of the tank, a wave force mitigation method is employed. The shaded area in Figure 2 represents the N-S computational domain established according to this method. Its dimensions are symmetric around both front-back and left-right directions of the numerical wave tank, measuring $5 \times 2.4 \times 6$ m. Waves propagate along positive x-axis. The SST K-Omega turbulence model is utilized for numerical simulations. The density and dynamic viscosity for water are 1025.0 kg/m^3 and $8.8871 \times 10^{-4} \text{ Pa}\cdot\text{s}$, respectively, while for air, they are 1.18415 kg/m^3 and $1.85508 \times 10^{-5} \text{ Pa}\cdot\text{s}$, respectively. Following the VOF wave meshing criteria recommended by STAR-CCM+ user's guide, the height of grid cells at free water surface is set to 1/20th of the wave height, and the width approximates 1/130th of the wave length. The final grid generation results of the numerical wave tank are shown in Figure 3. At the initial moment, waves exist in the region where $x < 0$, while the free surface remains stationary in the region where $x > 0$ to simulate the state where waves are just encountering the floating platform. The initial flow field is depicted in Figure 4. Finally, the time step adopted for the numerical simulation equals 0.004 s based on recommended calculation formula provided by STAR-CCM+ user's guide.

Utilizing the well-established numerical wave tank, the simulation of regular waves with a height of 0.12 m and a period of 1.414 s is initiated. The wave height at the coordinate origin is monitored, and subsequently, the calculated value for wave heights is obtained by averaging the last 10 periods of a stable segment in terms of wave height. The comparison between the calculated wave height and its theoretical value is depicted in Figure 5a. The statistical results reveal that the simulated wave height is approximately 0.11132 m, indicating a significant attenuation of 7.2% compared to the theoretical value, showing a relatively large error. To address this issue, adjustments are made to the input parameters related to wave height, resulting in improved accuracy, as shown in Figure 5b. At this stage, the calculated wave height reaches 0.11975 m with only an attenuation of 0.2% when compared to the theoretical value, meeting computational error requirement.

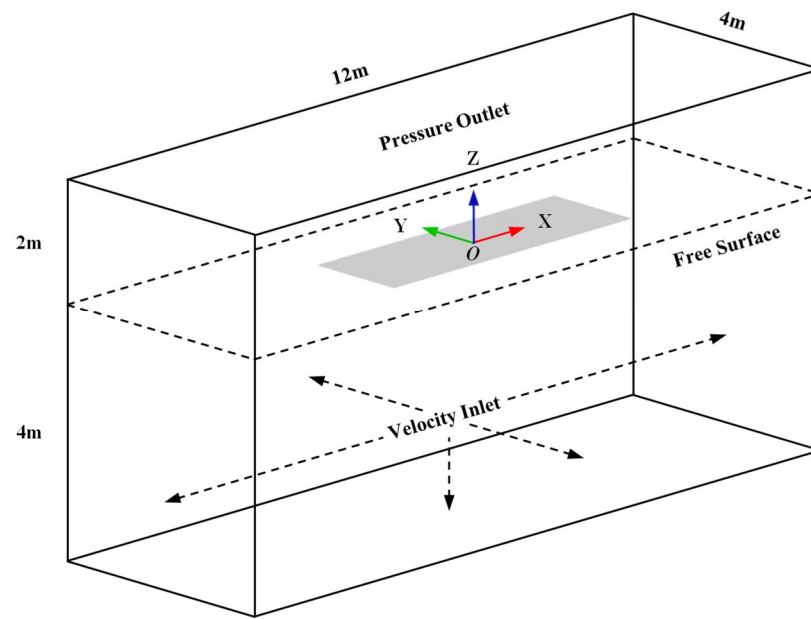


Figure 2. Three-dimensional numerical wave tank.

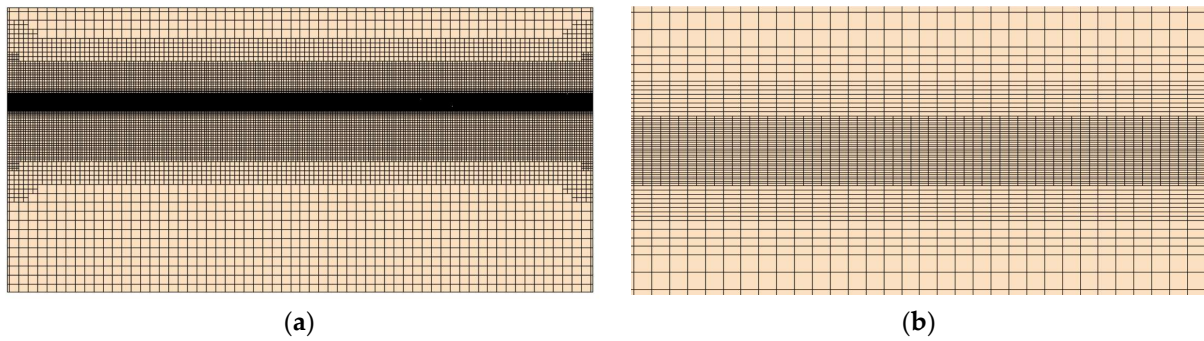


Figure 3. Grid generation results of the numerical wave tank. (a) Entire wave tank; (b) free surface.

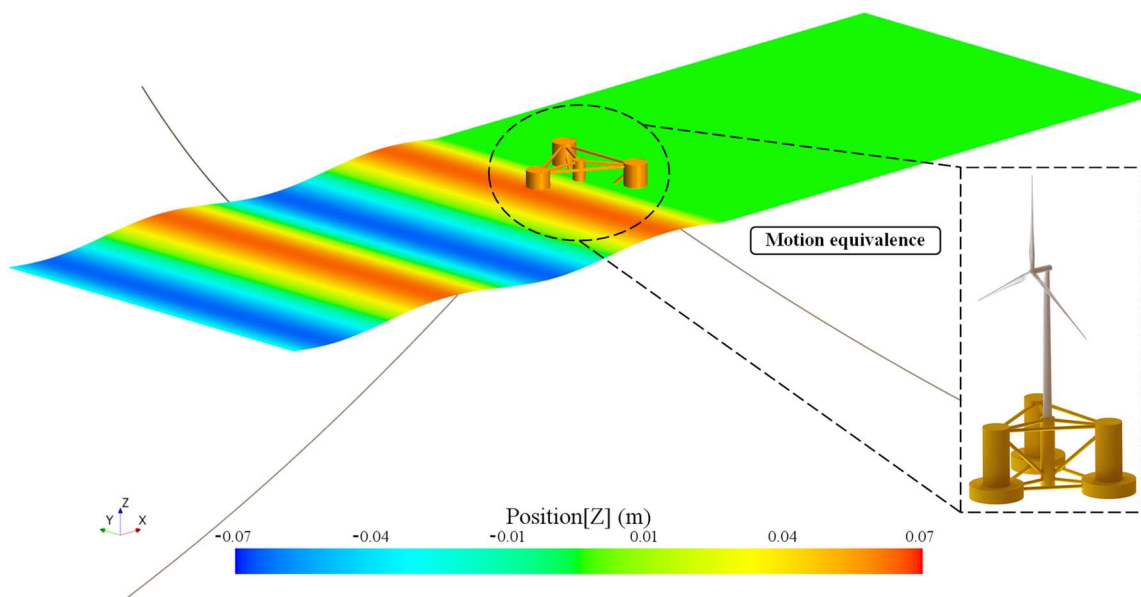


Figure 4. Initial flow field.

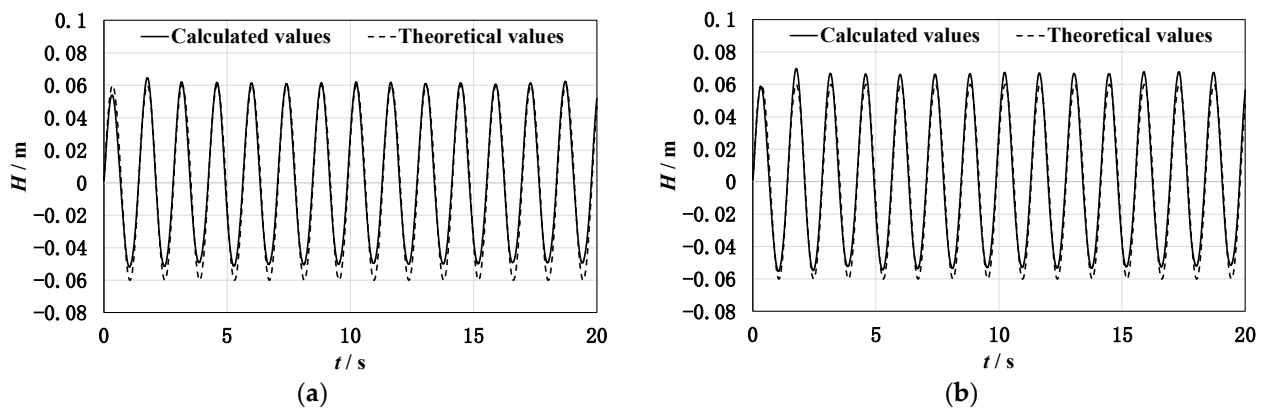


Figure 5. Calculated values and theoretical values of regular waves before and after correction. (a) Before correction; (b) after correction.

3.2. Platform Model

Li et al. from Shanghai Jiao Tong University took the DeepCwind semi-submersible platform proposed in the OC4 project as the research object and carried out model test research at Shanghai Jiao Tong University. The DeepCwind model used in this paper was consistent with the research object in the model test, and the numerical model verification was conducted based on the model test results. After obtaining the geometric model of the platform, a scaled-down version of the DeepCwind semi-submersible platform is created at a 1:50 ratio, following Froude number similitude. To control the position and motion amplitude of the platform in waves, three mooring lines are installed at each offset column’s base with angles of 120° between them. The parameters of both the scaled platform and mooring lines are detailed in Tables 2 and 3, respectively, with additional parameters referenced from Robertson et al.’s paper [25]. The experimental model used at Shanghai Jiao Tong University includes a wind turbine. However, this study does not simulate the wind field. Instead, the mass of wind turbine is included in the platform to achieve motion equivalence, and a comparison is made between the motion results of this study and those obtained from model tests conducted at Shanghai Jiao Tong University. The DeepCwind model and grid used in the computations are illustrated in Figure 6.

Table 2. Main parameters of scaled platform.

Parameters	Value
Draft (m)	0.4
Mass (kg)	112.15040
CM location below SWL (m)	0.19295
Roll inertia about CM (kg·m ²)	25.6352
Pitch inertia about CM (kg·m ²)	25.6352
Yaw inertia about CM (kg·m ²)	44.5120

Table 3. Main parameters of scaled mooring lines.

Parameters	Value
Number of mooring lines	3
Angle between adjacent lines (°)	120
Depth to anchors below SWL (m)	4
Depth to fairleads below SWL (m)	0.28
Radius to anchors from platform centerline (m)	16.752
Radius to fairleads from platform centerline (m)	0.81736
Unstretched mooring line length (m)	16.71
Mass per unit length (dry weight) (kg/m)	0.04534
EA of mooring line (N)	6028.8

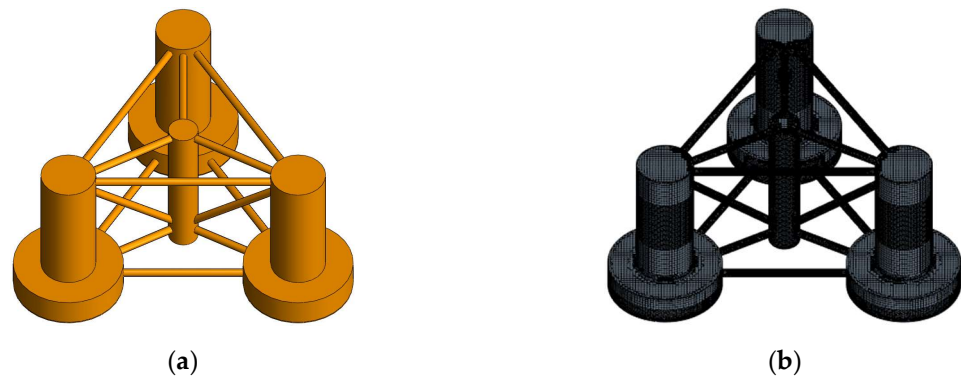


Figure 6. DeepCwind model and grid. (a) DeepCwind model; (b) DeepCwind grid.

After acquiring the scaled model, damping plates with a thickness of 4 mm and sizes of 0.04 m, 0.08 m, and 0.12 m are affixed at the base of each offset column. Herein, the sizes (referred to as ' L_h ') denote the increased distance along the radius of the offset column. The semi-submersible platform model with damping plate sizes of 0.12 m is illustrated in Figure 7.

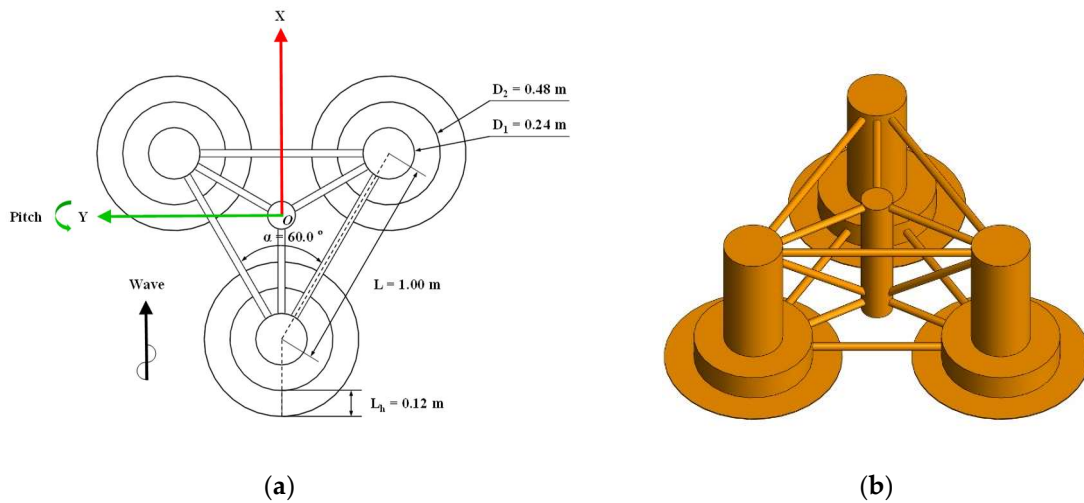


Figure 7. Semi-submersible platform model with a size of 0.12 m for damping plates. (a) Plan view; (b) side view.

In the calculation of STAR-CCM+, it is necessary to input the mass of the platform. This mass is computed by subtracting the sum of forces exerted along the z-axis by the three mooring lines from the buoyancy force on the platform monitored in calm water, then divided by gravitational acceleration. The calculated masses for platforms with varying damping plate sizes are comprehensively presented in Table 4. Besides damping plate sizes, and platform masses, other parameters such as the draft, center of gravity, and moment of inertia remain consistent across different platforms.

Table 4. Platform mass of different damping plate sizes.

L_h (m)	Mass (kg)
0	112.15040
0.04	112.95184
0.08	113.88239
0.12	114.93578

3.3. Flow Field Model

Utilizing the well-established numerical wave tank employed previously, the Deep-Cwind semi-submersible platform model is positioned at the coordinate origin, followed by grid partitioning. To accurately compute turbulent flow within the boundary layer, a prism layer consisting of 10 layers with a growth rate of 1.4 and a total thickness of 0.014 m is implemented. The values of non-dimensional wall distance y^+ on the surface of the platform during the final calculation are depicted in Figure 8. Notably, it can be observed that the values of y^+ at the damping plate deviate from the middle region ($5 < y^+ < 30$), as highlighted in Kalitzin et al.'s paper [26], thereby ensuring the accuracy of the numerical simulation.

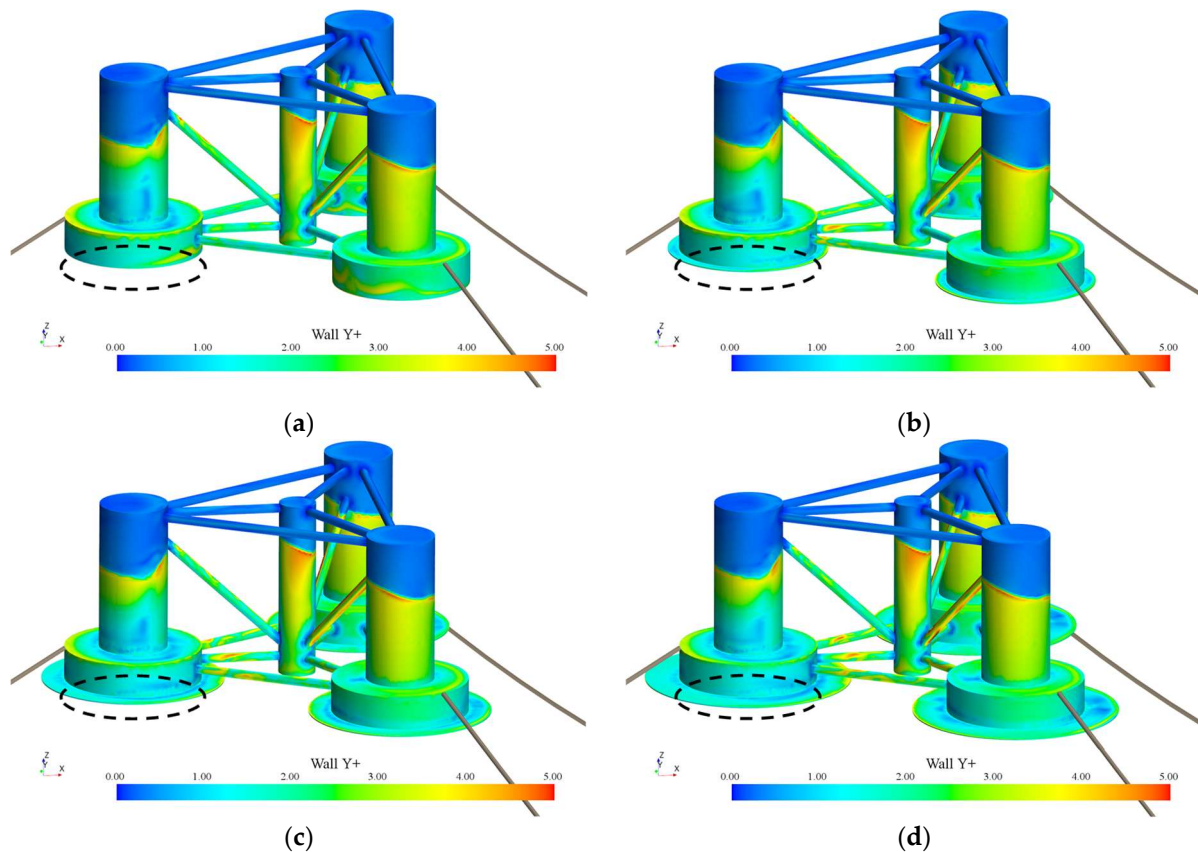


Figure 8. Surface y^+ values of each platform. (a) $L_h = 0$ m; (b) $L_h = 0.04$ m; (c) $L_h = 0.08$ m; (d) $L_h = 0.12$ m.

Concurrently, aiming to better capture the vortex process at the edge of the damping plates, a ring-shaped refinement zone is established surrounding the damping plates. This refinement zone has a circular cross-section and the center of the section is set at the bottom edge of the damping plates, with a radius equal to sizes of the damping plates. The radius of the section without a damping plate matches the minimum size of the damping plate. The final grid refinement results for both refined zones around each platform and overall grid are depicted in Figure 9.

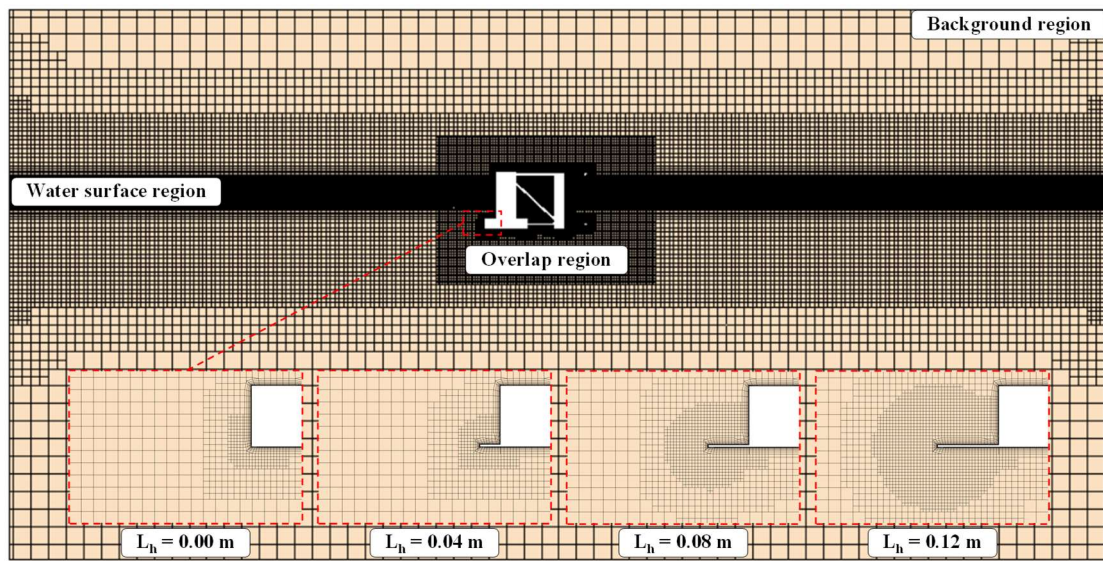


Figure 9. Grid refinement results.

3.4. Verification and Validation

Prior to simulating the pitch motion of the DeepCwind semi-submersible platform in regular waves, a convergence analysis is conducted on the numerical model. The simulation involves the free decay of pitch motion for the DeepCwind semi-submersible platform, commencing from an initial angle of 8.55° . To facilitate comparison with the experimental results provided by Li et al. [13], full-scale data are provided through the free decay motion. In order to verify time step independence, three different time steps of 0.002 s, 0.004 s, and 0.008 s are employed, and their corresponding results are illustrated in Figure 10a. For grid quantity independence verification, three grid partitioning schemes are generated by adjusting the base size resulting in grid quantities of 9 million, 6 million, and 3 million, and the results are presented in Figure 10b. As pointed out in Burmester et al. [27], the values of the first negative peaks in each simulation can be used for verification study since pitch motions are closely identical. The values of negative peaks for various time steps and grid quantities can be found in Tables 5 and 6, respectively. In order to ensure both accuracy and computational efficiency, a time step of 0.004 s along with a grid quantity of 6 million is selected for subsequent calculations.

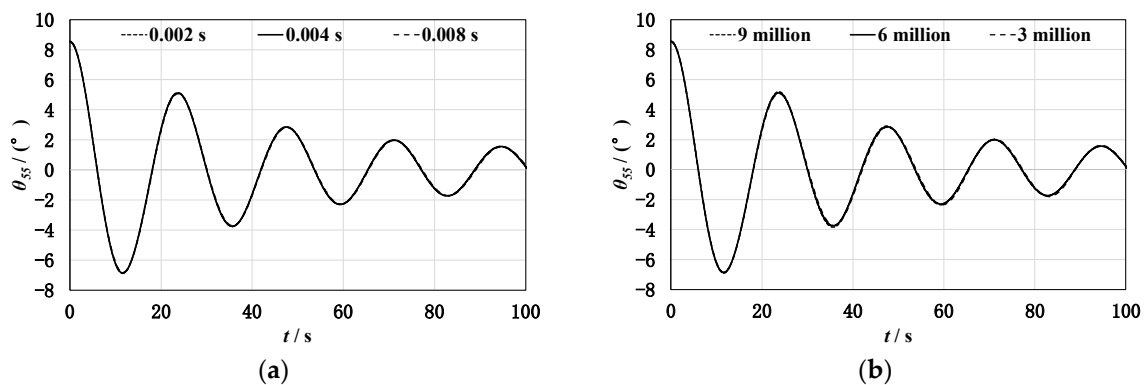


Figure 10. Pitch free decay motion time history from numerical simulations with different time steps and grid quantities. (a) Different time steps; (b) different grid quantities.

Table 5. First negative peaks for different time steps.

Time Step (s)	0.002	0.004	0.008
Peak value (°)	−6.878	−6.869	−6.814
Relative error (%)	0	−0.13	−0.93

Table 6. First negative peaks for different grid quantities.

Grid Quantity (Million)	9	6	3
Peak value (°)	−6.898	−6.869	−6.857
Relative error (%)	0	−0.42	−0.59

Following the convergence analysis, in order to validate the accuracy of the CFD method’s results, a comparison is conducted with Li et al.’s [13] experimental results, corresponding to the fourth step in Figure 1. The comparison between calculated and experimental values is depicted in Figure 11. It is observed that during the first period, the numerical simulation of pitch free decay aligns well with the experimental results. However, starting from the second period, due to accumulated errors caused by discretization, the free decay period in the numerical simulation becomes shorter compared to that observed in the model test. Nevertheless, the motion amplitudes are relatively consistent between both. The free decay period and the peak values during the final period are presented in Table 7 for both the numerical simulation and the model test, where the free decay period is calculated based on an average of the final three periods. The relative error demonstrates that the accuracy of the numerical model satisfies requirements for subsequent computations.

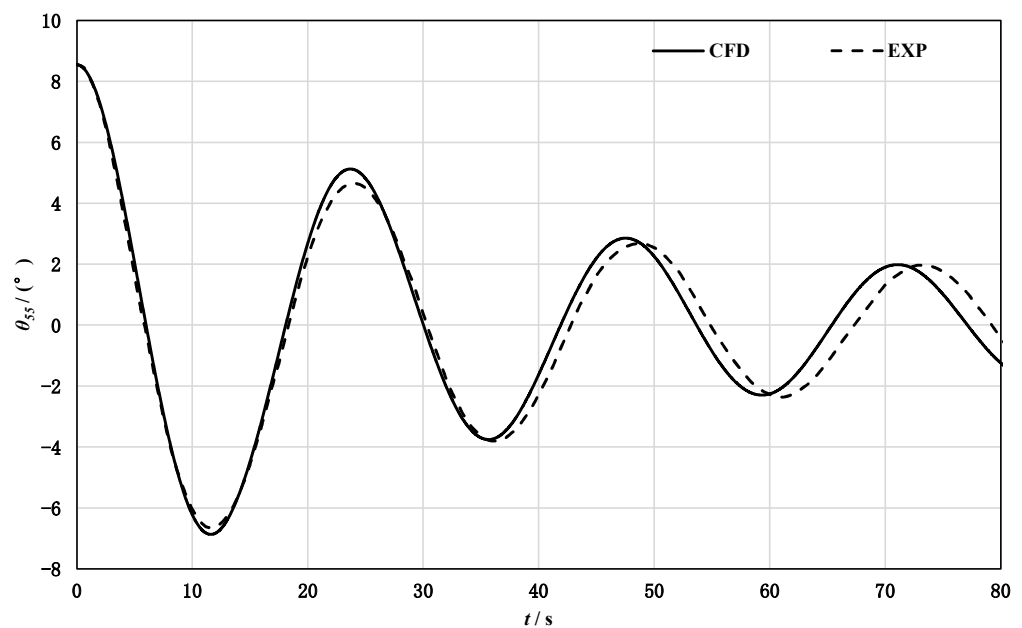


Figure 11. Comparison between calculated and experimental values of pitch free decay motions.

Table 7. Comparison between numerical simulation and model test.

Parameters	CFD	EXP	Relative Error (%)
Free decay period (s)	23.6	24.6	−4.07
Peak value of the last period (°)	1.985	1.962	1.17

4. Results and Discussion

Based on the numerical models and different platforms presented in Section 3, a series of CFD simulations are conducted. Firstly, distinct platforms undergo forced pitch motion in calm water to investigate the impact of damping plate size on the platform’s added moment of inertia and damping coefficient. Secondly, simulations are performed for the 1-DOF pitch motion of various platforms in regular waves, studying the effects of damping plate size on the platform’s pitch motion response and the resultant wave-induced loads. Finally, in regular waves, the platforms are immobilized, and their applied moments are monitored to explore methods for reducing wave-induced loads on them. Information for all cases is provided in Table 8.

Table 8. Case information.

Case No.	L_h (m)	Amplitude ($^\circ$)	Period (s)	Platform Draft (m)
1	0	5	1.414	0.40
2	0.04	5	1.414	0.40
3	0.08	5	1.414	0.40
4	0.12	5	1.414	0.40
5	0	1-DOF motion	1.414	0.40
6	0.04			0.40
7	0.08			0.40
8	0.12			0.40
9	0	1.499	1.414	0.40
10	0.04	1.672	1.414	0.40
11	0.08	1.873	1.414	0.40
12	0.12	2.025	1.414	0.40
13	0.12	Fixed platform		0.40
14	0.12			0.49

4.1. Forced Motion Results

To investigate the impact of damping plate size on added moment of inertia and damping coefficient, platforms firstly undergo forced motions in calm water, corresponding to Case 1–Case 4. During forced motion, the platform’s motion followed Equation (10), with the rotation center at the platform’s center of gravity. The pitch angle amplitude is set at 5° , and the pitch motion period is consistent with the subsequently calculated wave period of 1.414 s. Figure 12 illustrates pitch moment experienced by damping plates of different cases during forced motion. Data are collated from 5 periods within a stable segment ranging from 3 s to 11 s. Figure 13 illustrates the statistical results of moment for the various platforms and damping plates in forced motions. Tables 9 and 10 list the corresponding non-dimensional added moment of inertia and damping coefficients.

Table 9. A_{55}^* and B_{55}^* of different platforms in forced motion.

L_h (m)	A_{p55}^*	B_{p55}^*
0	0.00367	0.00193
0.04	0.00664	0.00488
0.08	0.01039	0.00871
0.12	0.01523	0.01308

Table 10. A_{55}^* and B_{55}^* of different damping plates in forced motion.

L_h (m)	A_{h55}^*	B_{h55}^*
0	0.00000	0.00000
0.04	0.00179	0.00183
0.08	0.00459	0.00491
0.12	0.00867	0.00865

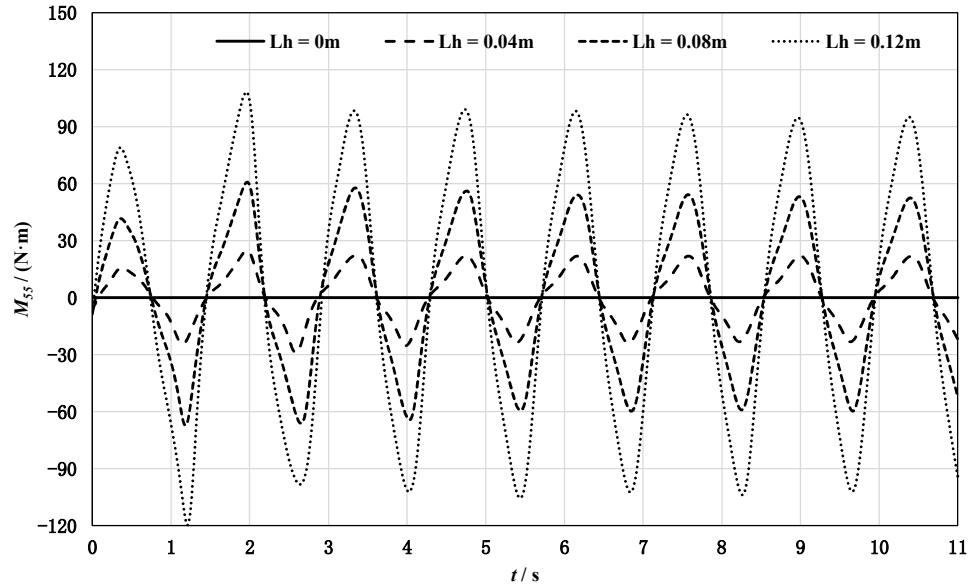


Figure 12. Pitch moment experienced by the damping plates of different cases during forced motion.

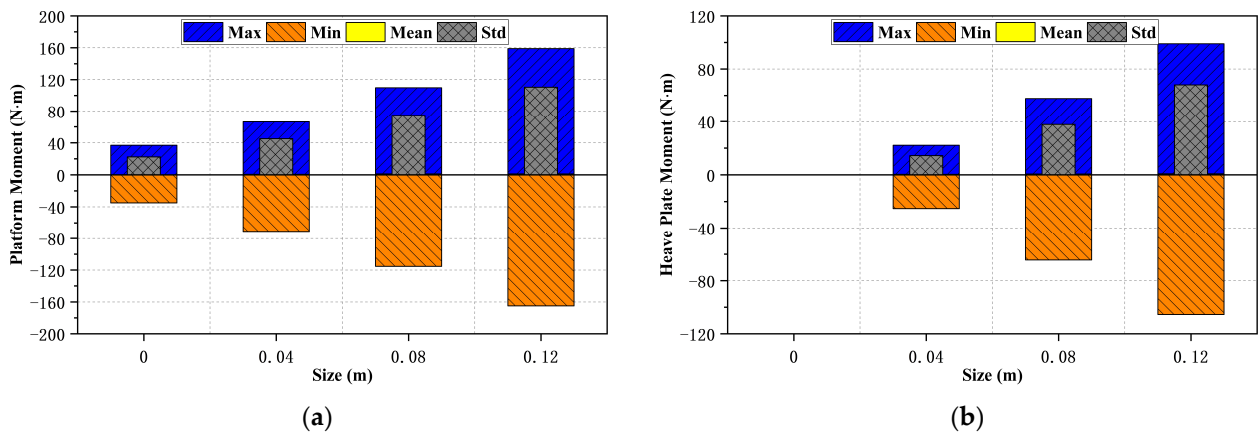


Figure 13. Pitch moment of different cases in forced motion. (a) Platform; (b) damping plate.

Inspecting Figure 13, it can be observed that when the platform undergoes forced motion, the pitch moment acting on both the platform and the damping plate increases with the size of the damping plate. At the same time, due to the symmetry of the forced motion, the average value of the moment is approximately equal to 0.

Tables 9 and 10 demonstrate a gradual increase in both the added moment of inertia and damping coefficients for the platform and damping plate as the size of the damping plate increases. In accordance with Equation (12), under constant moment exerted on the platform for pitch motion, an increase in the added moment of inertia and damping coefficients would lead to a reduction in the platform’s pitch angle.

Figure 14 illustrates the wave surface conditions for different cases at 11 s. The red area represents wave heights above 0.007 m, while the blue area denotes wave heights

below -0.007 m. Importantly, with the increase in damping plate size, there is an amplified disturbance observed on the wave surface. This indicates that the damping plate is relatively close to the water surface, and the presence of waves may increase the wave-induced loads on the damping plate.

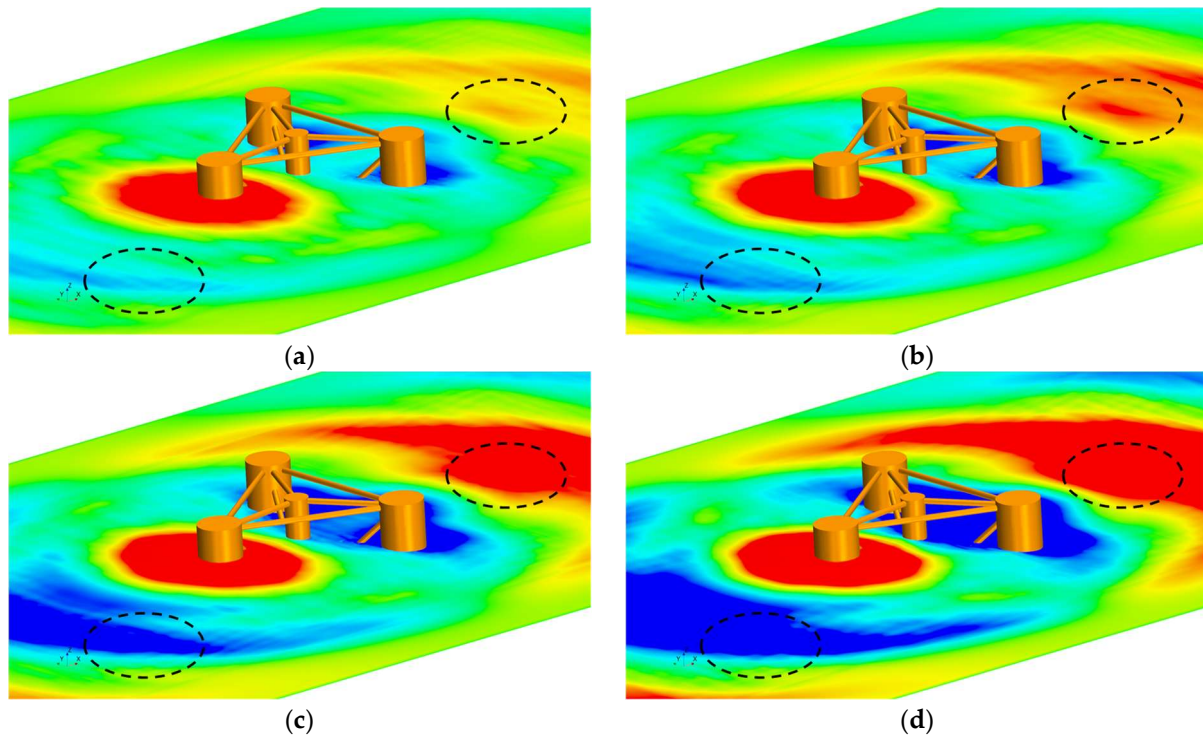


Figure 14. Free surface elevations of different cases under forced motion. (a) $L_h = 0$ m; (b) $L_h = 0.04$ m; (c) $L_h = 0.08$ m; (d) $L_h = 0.12$ m.

4.2. 1-DOF Motion Results

After evaluating the influence of damping plate size on the added moment of inertia and damping coefficients through forced motion analysis, simulations are conducted for the 1-DOF pitch motion of different platforms in regular waves, corresponding to Case 5–Case 8. This aimed to investigate the impact of damping plate size on platform's pitch motion response and resulting wave-induced loads. Figure 15 illustrates the pitch motion response of different platforms. It is worth noting that the platform's pitch motion stabilizes between 12 and 20 s. Therefore, data from this specific timeframe spanning across five periods are selected for subsequent analysis.

Upon acquiring the necessary data, in accordance with the methodology outlined in Section 2.3, the non-dimensional added moment of inertia and damping coefficients are calculated for various platforms and damping plates. The moment fitting results for the platform and damping plate with a size of 0.12 m are depicted in Figure 16. Figures 17 and 18 illustrate the statistical results of pitch angles of different cases and the moment of various platforms and damping plates during 1-DOF motions. Tables 11 and 12 list the corresponding non-dimensional added moment of inertia and damping coefficients, facilitating subsequent quantitative analysis. The growth rate signifies the coefficient growth rate for other platforms relative to the platform without a damping plate. The proportion indicates the ratio between respective damping plate coefficients and platform coefficients.

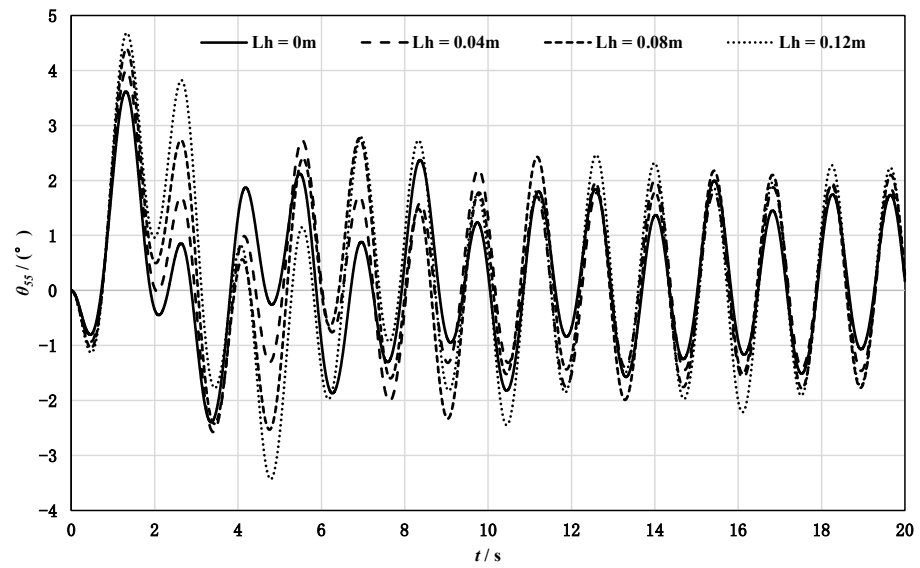


Figure 15. Pitch motion response of different platforms.

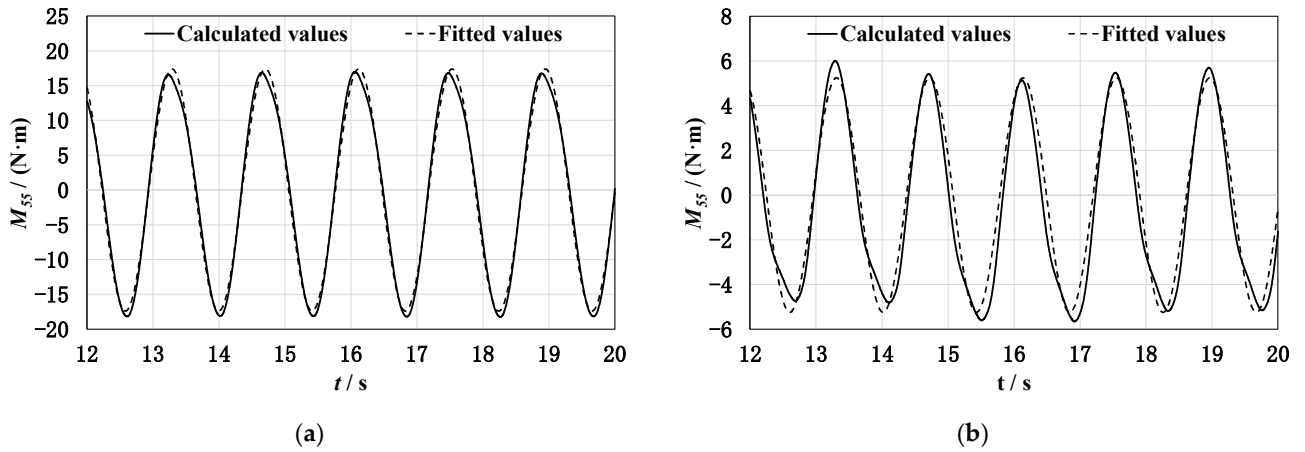


Figure 16. Pitch moment fitting results for platform and damping plates with a size of 0.12 m. (a) Pitch moment acting on platform and damping plates; (b) pitch moment acting on damping plate only.

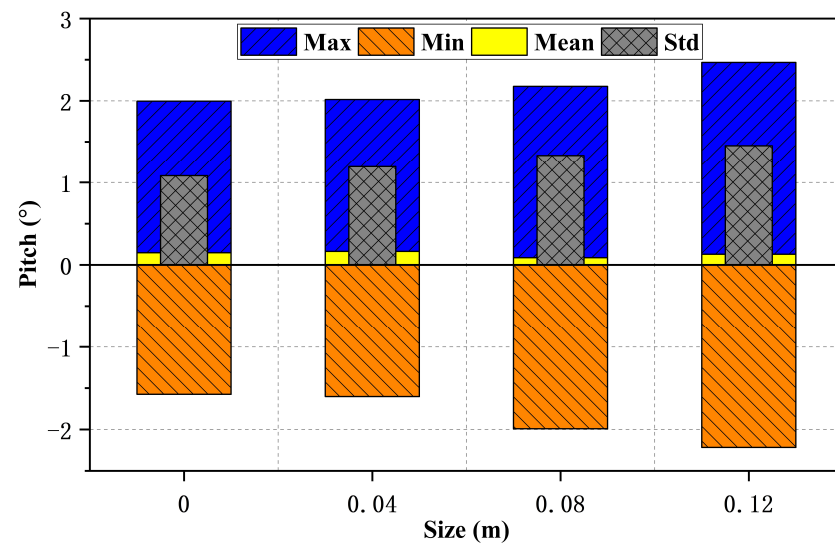


Figure 17. Pitch angle of different cases in 1-DOF motion.

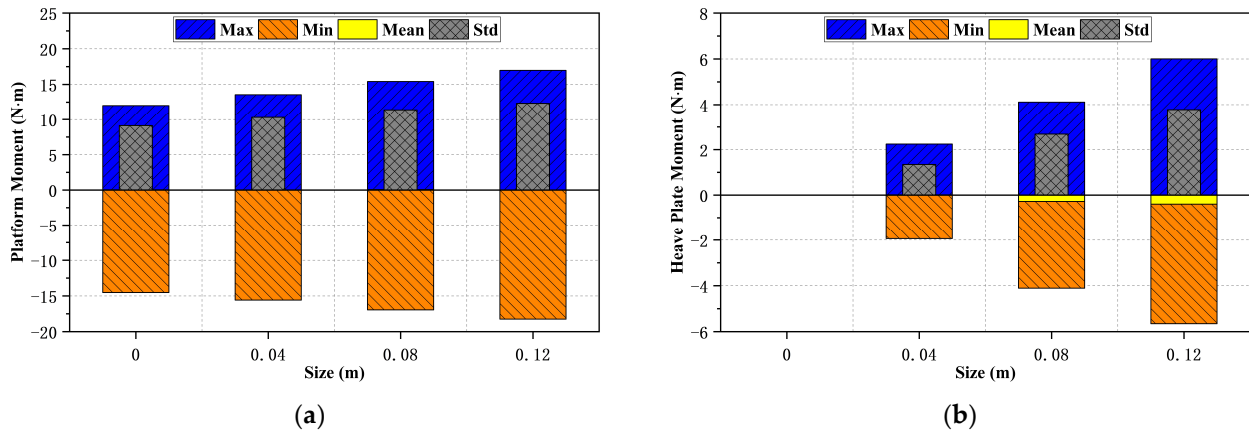


Figure 18. Pitch moment of different cases in 1-DOF motion. (a) Platform; (b) damping plate.

Table 11. A_{55}^* and B_{55}^* of different platforms in 1-DOF motion.

L_h (m)	A_{p55}^*	Growth Rate (%)	B_{p55}^*	Growth Rate (%)
0	0.00316	0	0.00439	0
0.04	0.00325	2.85	0.00443	0.91
0.08	0.00339	7.28	0.00428	-2.51
0.12	0.00345	9.18	0.00423	-3.64

Table 12. A_{55}^* and B_{55}^* of different damping plates in 1-DOF motion.

L_h (m)	A_{h55}^*	Proportion (%)	B_{h55}^*	Proportion (%)
0	0.00000	0	0.00000	0
0.04	0.00026	8.00	0.00064	14.45
0.08	0.00063	18.58	0.00107	25.00
0.12	0.00092	26.67	0.00135	31.91

4.2.1. Influence of Installing Damping Plates on the Platform

Figure 19 illustrates a comparison of the non-dimensional added moment of inertia and damping coefficients between the case without a damping plate and the case with a damping plate size of 0.04 m. Based on Tables 11 and 12, it is evident that upon installation of the damping plate, both the platform’s added moment of inertia and damping coefficients exhibit a slight increase compared to those without the plate. Additionally, the non-dimensional added moment of inertia and damping coefficients contributed by the damping plate, respectively, account for 8.00% and 14.45% of their corresponding values for the platform.

Figure 20 illustrates the pitch motion responses for the cases without a damping plate and with a damping plate size of 0.04 m. By integrating information from Figures 17 and 18a, it is observed that the installation of the damping plate leads to an increase in both the amplitude of platform’s pitch motion and the maximum and minimum moment values. This finding contradicts the inference made in Section 4.1, indicating that while augmenting the platform’s added moment of inertia and damping coefficients, the damping plate significantly amplifies wave-induced loads acting on the platform, thereby elevating its pitch motion amplitude.

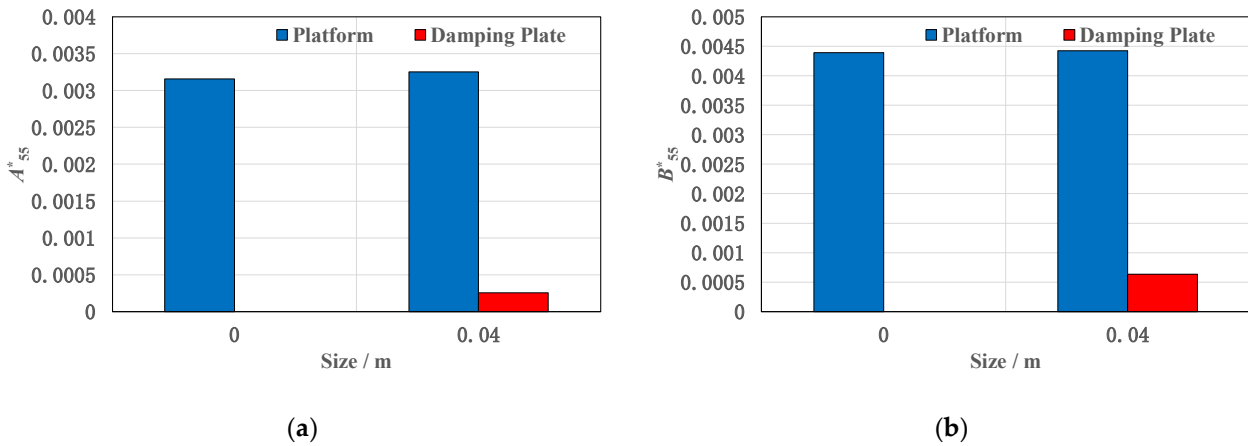


Figure 19. Non-dimensional added moment of inertia and damping coefficients without and with damping plates. (a) Non-dimensional added moment of inertia; (b) non-dimensional damping coefficients.

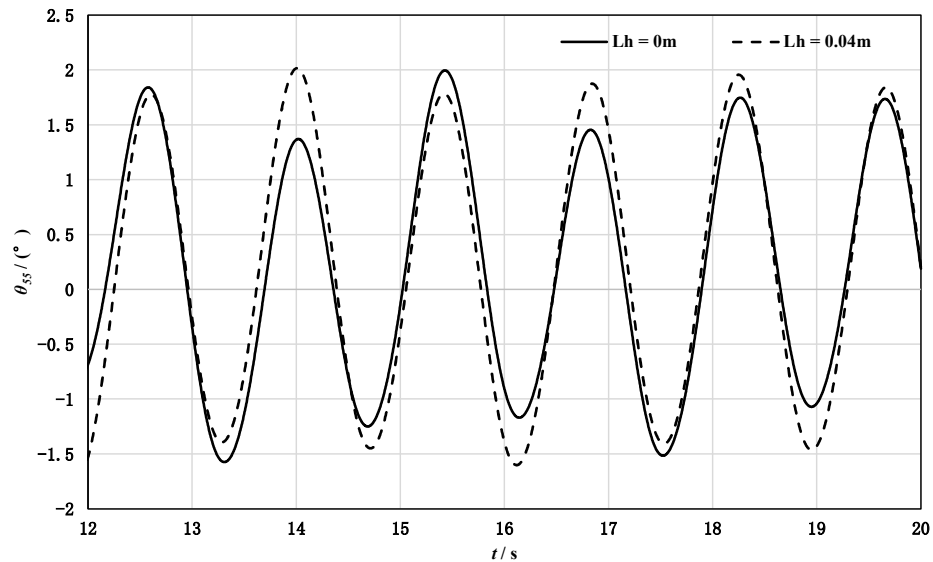


Figure 20. Pitch motion responses before and after installing damping plate.

4.2.2. Influence of Different Damping Plate Sizes on the Platform

Figure 21 illustrates the non-dimensional added moment of inertia and damping coefficients for different platforms and damping plates. It is evident that the platform’s added moment of inertia gradually increases with the increasing size of the damping plate, while the damping coefficient exhibits an initial increase followed by a decrease trend. Simultaneously, both the damping plate’s added moment of inertia and damping coefficients progressively increase with the size. According to Table 12, as the size increases, there is an increasing proportion of damping plate’s added moment of inertia and damping coefficients within the platform. It is clear that varying sizes of damping plates have distinct effects on the platform’s added moment of inertia and damping coefficients, and these effects become more pronounced as the size increases.

Table 13 presents the ratio of corresponding coefficients for forced and 1-DOF motion of platforms and damping plates. It can be observed that both the added moment of inertia and damping coefficients of the damping plate for forced motion in calm water are greater than those for 1-DOF motion in regular waves. Similar trends are also observed for the platform’s corresponding coefficients. However, when there is no damping plate present, the damping coefficient of the platform for forced motion is lower compared to that for 1-DOF motion.

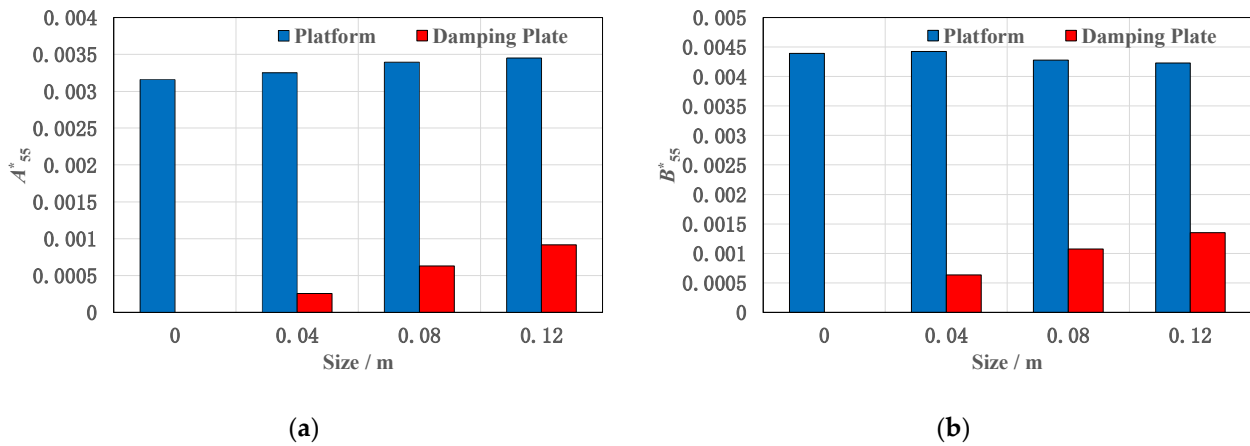


Figure 21. Non-dimensional added moment of inertia and damping coefficients for different platforms and damping plates. (a) Non-dimensional added moment of inertia; (b) non-dimensional damping coefficients.

Table 13. A_{55}^* and B_{55}^* ratio of forced motion and 1-DOF motion.

L_h (m)	A_{p55}^* Ratio	B_{p55}^* Ratio	A_{h55}^* Ratio	B_{h55}^* Ratio
0	1.16	0.44	0	0
0.04	2.04	1.10	6.88	2.86
0.08	3.06	2.04	7.29	4.59
0.12	4.41	3.09	9.42	6.41

The relationship between the non-dimensional added moment of inertia and damping coefficients of different damping plates with their outer circumference (C) for forced and 1-DOF motion is depicted in Figure 22. It can be observed that, irrespective of the type of motion, a linear relationship exists between the added moment of inertia and damping coefficients of the damping plates with respect to their outer circumferences.

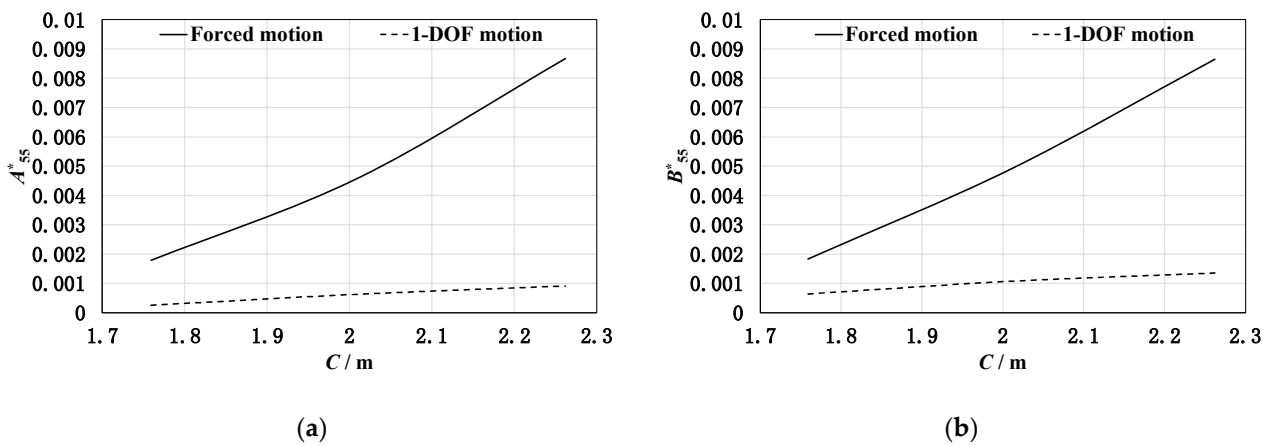


Figure 22. Fitting results of non-dimensional added moment of inertia and damping coefficient for different damping plates. (a) Non-dimensional added moment of inertia; (b) non-dimensional damping coefficients.

Relevant studies [28] suggest that the primary mechanism underlying damping generation is the dissipation of kinetic energy during the shedding of vortices in structural motion. In wind turbine foundation structures, a higher number of generated and shed vortices during their movement leads to increased energy dissipation, thereby enhancing damping performance. Research carried out by Jiang et al. [29] indicates that it is easy for

the sharp edge of the damping plate to cause a large amount of vortex shedding, and a longer shape edge causes a larger amount of flow separation and dissipates more energy into the surrounding fluid. Figure 23 illustrates the three-dimensional vortex field near different cases at the final trough of the 1-DOF pitch motion responses (corresponding to 18.948 s). The evidence suggests that an increase in size leads to a noticeable rise in the generation and shedding of vortices near the damping plate. Therefore, we find in Figure 23 that the vortices on the damping plate increases significantly with the increase in size. Furthermore, due to the positive wave propagation along the x-axis and the distribution of two offset columns on the right side, there are more visible vortices around the right-side damping plate compared to the left-side counterpart, with most shed vortices concentrated between the two damping plates on the right side. Figure 23d also shows the comparison of vorticity of different fluid models. It can be seen that the inviscid model cannot capture vorticity. The hydrodynamic load of the damping plate mainly comes from vorticity, and the lack of vorticity indicates the capture uncertainty, so it is necessary to use the viscous model for calculation.

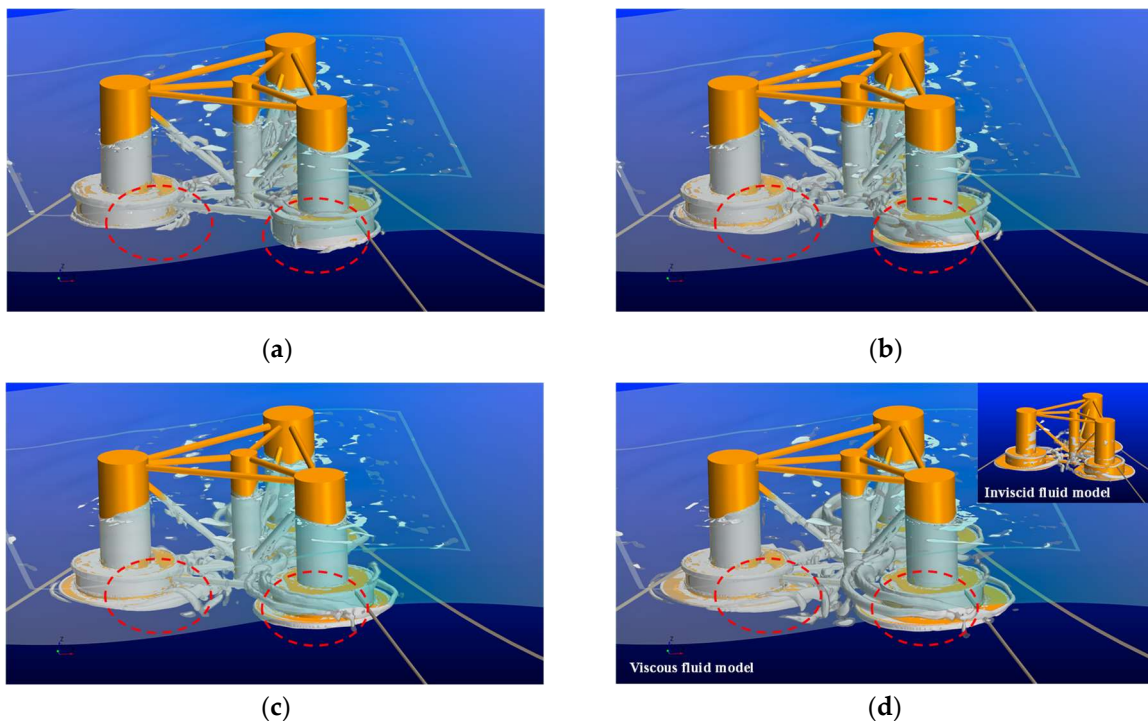


Figure 23. Vortex field near different cases of 1-DOF motion. (a) $L_h = 0$ m; (b) $L_h = 0.04$ m; (c) $L_h = 0.08$ m; (d) $L_h = 0.12$ m.

Figure 24 illustrates the three-dimensional vortex field near different cases at the last trough of the forced motion responses (corresponding to 10.96 s). It can be observed that, compared to 1-DOF motion, similar patterns are followed by vortex generation and shedding around the damping plate during forced motion, but there is a significantly higher quantity of shed vortices. This is also the reason why the added moment of inertia and damping coefficients during forced motion are greater than those during 1-DOF motion.

Figure 25 illustrates the pitch motion response of various platforms, while Tables 14 and 15 compare the average pitch angle amplitude and parameter growth rates among these platforms. It is evident that an increase in damping plate size leads to a corresponding increase in platform pitch angle amplitude. Notably, this is opposite to the effect of damping plate size on the platform’s heave motion response, that is, by increasing the diameter of the damping plates, the heave motion response of the platform can be reduced [30]. Furthermore, Tables 11 and 15 reveal that the moment acting on the platform increases

with increasing damping plate size, and this increment being more pronounced compared to the rise in the added moment of inertia.

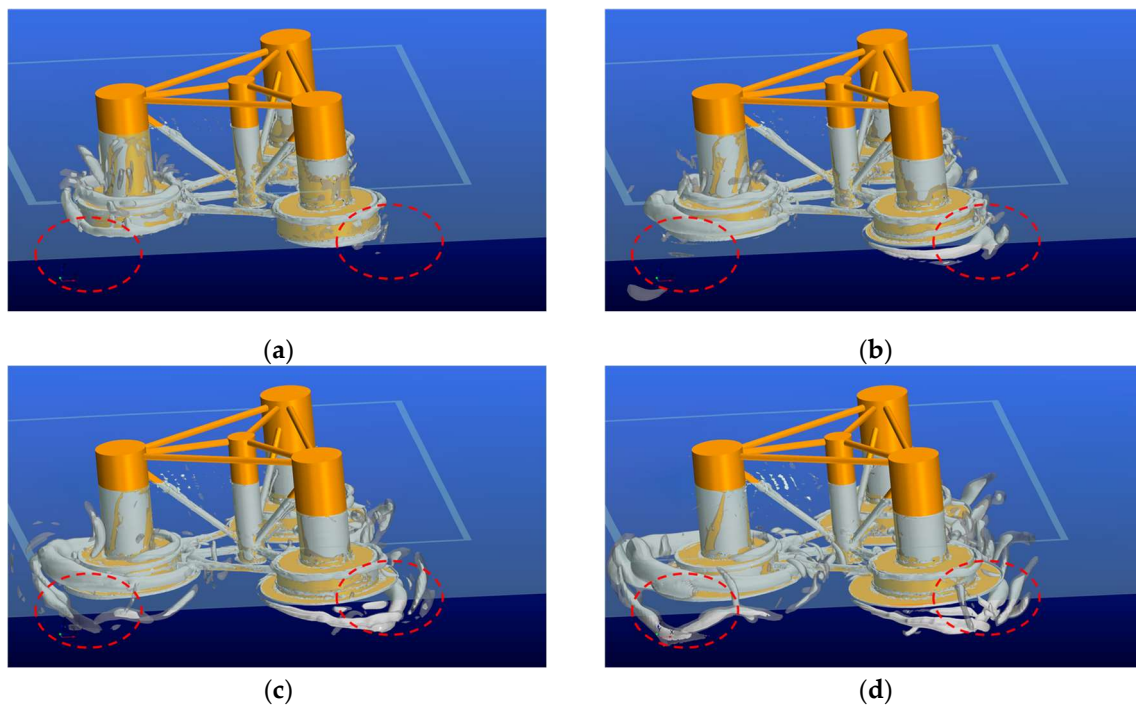


Figure 24. Vortex field near different cases of forced motion. (a) $L_h = 0$ m; (b) $L_h = 0.04$ m; (c) $L_h = 0.08$ m; (d) $L_h = 0.12$ m.

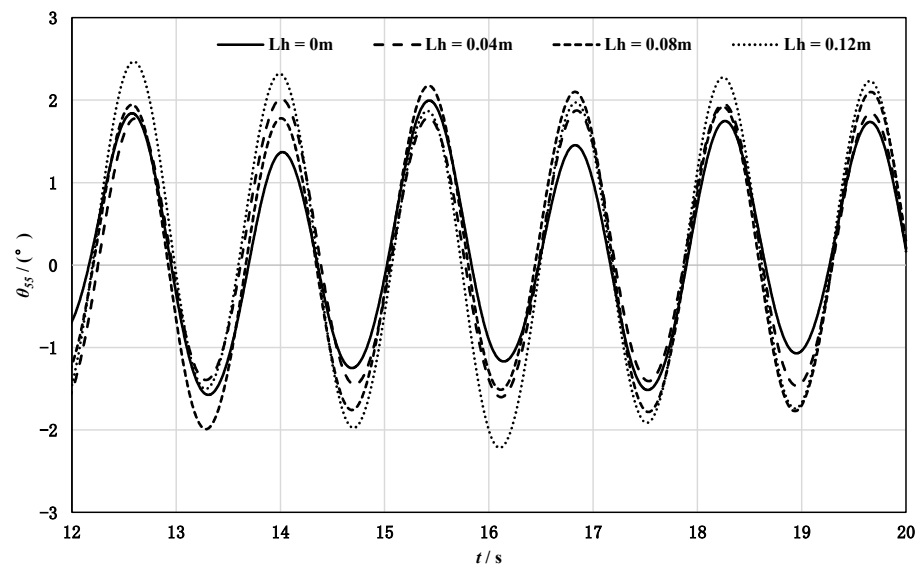


Figure 25. Pitch motion response of platforms with different damping plates between 12 and 20s.

Table 14. Average pitch angle amplitude of different platforms.

L_h (m)	Average Pitch Angle Amplitude ($^{\circ}$)
0	1.499
0.04	1.672
0.08	1.873
0.12	2.025

Table 15. Different parameter growth rates of platforms in 1-DOF motion.

L_h (m)	A_{p55}^* Growth Rate (%)	B_{p55}^* Growth Rate (%)	Maximum Moment Growth Rate (%)	Minimum Moment Growth Rate (%)
0	0	0	0	0
0.04	2.85	0.91	12.70	7.35
0.08	7.28	−2.51	28.16	16.75
0.12	9.18	−3.64	41.12	25.65

After calculating the average amplitude of pitch angles for different platforms, these values are utilized as the pitch angle amplitudes for unequal amplitude forced motion, corresponding to Case 9–Case 12. All other parameters remain consistent with the earlier computations on equal forced motion. Table 16 illustrates the ratio of corresponding coefficients for unequal amplitude forced motion compared to 1-DOF motion in platforms and damping plates, while Table 17 demonstrates the ratio between equal and unequal amplitude forced motion in platforms and damping plates. Similar to equal forced motion, it is observed that without a damping plate, the damping coefficient of platforms during unequal amplitude forced motion in calm water is lower than that during 1-DOF motion in regular waves. Furthermore, both the added moment of inertia and damping coefficients for equal forced motion in platforms and damping plates are greater than those for unequal amplitude forced motion. Studies by Thiagarajan et al. [31] suggest that this discrepancy arises due to the larger amplitude of motion in equal forced motion compared to unequal amplitude forced motion. Based on Tables 13 and 16, it is evident that in the absence of a damping plate, the added moment of inertia for platforms subjected to unequal amplitude forced motions is nearly equivalent to that observed in platforms experiencing 1-DOF motions. However, with a damping plate, the added moment of inertia for platforms under unequal amplitude forced motions significantly exceeds that observed in platforms with 1-DOF motions. Nevertheless, under certain minor angular conditions like Case 11, the damping coefficient for platforms undergoing forced motion is approximately equal to that of platforms with 1-DOF motions. This implies that during the design of the damping plate, an appropriate choice of angle can aid in predicting the damping coefficient of platforms experiencing regular waves through forced motion in calm water.

Table 16. A_{55}^* and B_{55}^* ratio of unequal amplitude forced motion and 1-DOF motion.

L_h (m)	A_{p55}^* Ratio	B_{p55}^* Ratio	A_{h55}^* Ratio	B_{h55}^* Ratio
0	1.06	0.18	0	0
0.04	1.69	0.57	4.69	1.70
0.08	2.78	0.99	6.46	2.33
0.12	4.34	1.64	9.27	3.46

Table 17. A_{55}^* and B_{55}^* ratio of equal amplitude forced motion and unequal amplitude forced motion.

L_h (m)	A_{p55}^* Ratio	B_{p55}^* Ratio	A_{h55}^* Ratio	B_{h55}^* Ratio
0	1.10	2.47	0	0
0.04	1.21	1.94	1.47	1.68
0.08	1.10	2.05	1.13	1.97
0.12	1.02	1.89	1.02	1.85

4.3. Influence of Damping Plate Installation Depth on Wave Loads Acting on the Platform

In order to mitigate wave loads acting on the platform, a platform with a damping plate size of 0.12 m is affixed in regular waves and subsequently translated along the negative z-axis by 0.09 m. A comparative analysis is conducted between the magnitudes of moments experienced by the platform and damping plate before and after translation,

corresponding to Case 13 and Case 14, respectively. The calculation duration and data interval analyzed align consistently with forced motion, as shown in Tables 18 and 19. The results demonstrate that increasing the distance between damping plates and free surface significantly diminishes the wave loads acting on the platform, with all parameters of the moments on the platform and damping plate experiencing reductions exceeding 10%.

Table 18. Pitch moment of platforms before and after translation.

Parameters	Max	Min	Mean	Std. Dev.
Normal draft (N·m)	61.894	−65.957	1.328	45.840
Big draft (N·m)	55.397	−57.8	0.997	40.291
Reduction rate (%)	10.50	12.37	24.92	12.11

Table 19. Pitch moment of damping plates before and after translation.

Parameters	Max	Min	Mean	Std. Dev.
Normal draft (N·m)	34.228	−34.136	0.850	23.992
Big draft (N·m)	27.479	−27.206	0.589	19.216
Reduction rate (%)	19.72	20.30	30.71	19.91

Figure 26 illustrates the three-dimensional vortex field near the platform at 10.96 s in different drafts. According to the areas marked by three red circles, it is evident that, compared to the pre-translation vortex field, there is no significant reduction in the generation and shedding of vortices near the damping plate after increasing the distance between damping plates and free surface. This observation suggests that the installation depth of the damping plate is independent of the evolution of the vortex and increasing the installation depth of the damping plate effectively reduces wave loads acting on the platform without compromising its functionality.

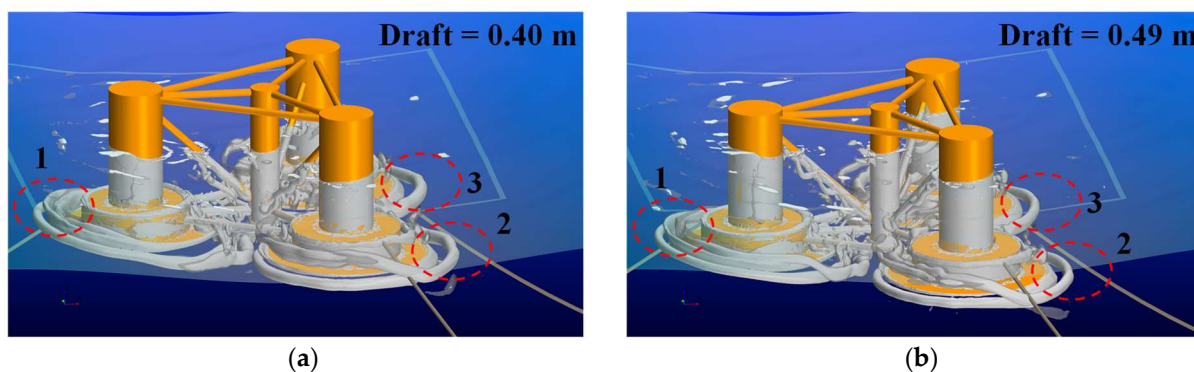


Figure 26. Vortex field near the platform in different drafts. (a) Before increasing the distance between damping plates and free surface; (b) after increasing the distance between damping plates and free surface.

5. Conclusions

This work conducts a numerical simulation study by using CFD method to analyze the impact of installing damping plates and their sizes on the pitch motion response of floating offshore wind turbine, and proposes optimization strategies for the damping plate design. The following conclusions can be drawn:

1. In calm water, an increase in damping plate sizes leads to gradual increments in both the added moment of inertia and damping coefficients of both the FOWT platform and damping plates during forced pitch motion.
2. Under regular wave conditions, increasing damping plate sizes results in a gradual increase in the added moment of inertia of the FOWT platform, while exhibiting an

initial increase followed by a decreasing trend for the damping coefficient. Simultaneously, the increase in wave loads surpasses the increase in added moment of inertia, leading to a progressive rise in the pitch motion response.

3. While installing damping plates increases the pitch motion's added moment of inertia and damping coefficients for FOWT platforms, simply increasing their sizes does not reduce the pitch motion response. It is essential to consider the increase in wave loads.
4. Increasing the installation depth of damping plates has little effect on the added moment of inertia and damping coefficient of the FOWT platform, but significantly decreases the wave-induced loads on the platform. The optimal design of the damping plate for floating offshore wind turbine should take into account both the size and the installation depth.

The study exclusively focused on the pitch motion response of the FOWT platform in regular waves. However, real waves often exhibit significant nonlinearity. Therefore, further investigation is imperative to explore the pitch motion response in irregular waves.

Author Contributions: Conceptualization, resources, supervision, project administration, and funding acquisition, J.L. and Y.J.; methodology and formal analysis, C.W. and Y.J.; software, validation, investigation, data curation, and visualization, C.W.; writing—original draft preparation, C.W. and Y.Y.; writing—review and editing, J.X. and G.T. All authors have read and agreed to the published version of the manuscript.

Funding: This work was supported by Shenzhen 2022 Key Project for Technological Research [grant number JSGG20220831110803006], Key technology research and demonstration project of 10 MW deep-sea floating offshore wind turbine (DTGD-2023-10174), and Key technology research task of floating offshore combined wind and wave power generation.

Institutional Review Board Statement: Not applicable.

Informed Consent Statement: Not applicable.

Data Availability Statement: The data presented in this study are available on request from the corresponding author.

Acknowledgments: The authors would like to express their gratitude to the editor and reviewers for their constructive comments and suggestions, which have contributed to the enhancement of the paper's quality.

Conflicts of Interest: Author Jie Xu was employed by the company Guangdong Datang International Chaozhou Power Generation Co., Ltd., and Yi Yang was employed by the company China Southern Power Grid Electric Power Technology Co., Ltd. The remaining authors declare that the research was conducted in the absence of any commercial or financial relationships that could be construed as a potential conflict of interest.

References

1. Ma, Y.; Chen, C.; Fan, T.; Lu, H. Research on the Dynamic Behaviors of a Spar Floating Offshore Wind Turbine With an Innovative Type of Mooring System. *Front. Energy Res.* **2022**, *10*, 853448. [[CrossRef](#)]
2. Wu, X.; Hu, Y.; Li, Y.; Yang, J.; Duan, L.; Wang, T.; Adcock, T.; Jiang, Z.; Gao, Z.; Lin, Z.; et al. Foundations of Offshore Wind Turbines: A Review. *Renew. Sustain. Energy Rev.* **2019**, *104*, 379–393. [[CrossRef](#)]
3. Srinivasan, C.; Serino, G.; Chauhan, Y.J.; Sanghvi, C.; Gohil, A. Feasibility Study of Offshore Triceratops-Supported Floating Offshore Wind Turbine. *J. Inst. Eng. (India) Ser. A* **2024**, *105*, 295–305. [[CrossRef](#)]
4. Chandrasekaran, S.; Chinu, P. Dynamic Analysis of Offshore Triceratops Supporting Wind Turbine: Preliminary Studies. *Marit. Technol. Res.* **2023**, *6*, 265564. [[CrossRef](#)]
5. Lopez-Pavon, C.; Souto-Iglesias, A. Hydrodynamic Coefficients and Pressure Loads on Heave Plates for Semi-Submersible Floating Offshore Wind Turbines: A Comparative Analysis Using Large Scale Models. *Renew. Energy* **2015**, *81*, 864–881. [[CrossRef](#)]
6. Koo, B.J.; Goupee, A.J.; Kimball, R.W.; Lambrakos, K.F. Model Tests for a Floating Wind Turbine on Three Different Floaters. *J. Offshore Mech. Arct. Eng.* **2014**, *136*, 020907. [[CrossRef](#)]
7. Goupee, A.J.; Koo, B.J.; Kimball, R.W.; Lambrakos, K.F.; Dagher, H.J. Experimental Comparison of Three Floating Wind Turbine Concepts. *J. Offshore Mech. Arct. Eng.* **2014**, *136*, 020906. [[CrossRef](#)]
8. Coulling, A.J.; Goupee, A.J.; Robertson, A.N.; Jonkman, J.M.; Dagher, H.J. Validation of a FAST Semi-Submersible Floating Wind Turbine Numerical Model With DeepCwind Test Data. *J. Renew. Sustain. Energy* **2013**, *5*, 023116. [[CrossRef](#)]

9. Li, L.; Hu, Z.; Wang, J.; Hu, Q. Dynamic Responses of a Semi-Type Offshore Floating Wind Turbine. In Proceedings of the ASME 2014 33rd International Conference on Ocean, Offshore and Arctic Engineering, San Francisco, CA, USA, 8–13 June 2014.
10. Hu, Z.; Li, L.; Wang, J.; Hu, Q.; Shen, M. Dynamic Responses of a Semi-Type Offshore Floating Wind Turbine During Normal State and Emergency Shutdown. *China Ocean Eng.* **2016**, *30*, 97–112. [[CrossRef](#)]
11. Chen, P.; Chen, J.; Hu, Z. Review of Experimental-Numerical Methodologies and Challenges for Floating Offshore Wind Turbines. *J. Mar. Sci. Appl.* **2020**, *19*, 339–361. [[CrossRef](#)]
12. Chen, C.; Ma, Y.; Fan, T. Review of Model Experimental Methods Focusing on Aerodynamic Simulation of Floating Offshore Wind Turbines. *Renew. Sustain. Energy Rev.* **2022**, *157*, 112036. [[CrossRef](#)]
13. Li, L.; Hu, Z.; Wang, J.; Ma, Y. Development and Validation of an Aero-Hydro Simulation Code for an Offshore Floating Wind Turbine. *Ocean Wind Energy* **2015**, *2*, 1–11.
14. Li, L.; Gao, Y.; Hu, Z.; Yuan, Z.; Day, S.; Li, H. Model Test Research of a Semisubmersible Floating Wind Turbine With an Improved Deficient Thrust Force Correction Approach. *Renew. Energy* **2018**, *119*, 95–105. [[CrossRef](#)]
15. Wang, Y.; Chen, H.C.; Vaz, G.; Burmester, S. CFD Simulation of Semi-Submersible Floating Offshore Wind Turbine Under Pitch Decay Motion. In Proceedings of the ASME 2019 2nd International Offshore Wind Technical Conference, St. Julian's, Malta, 3–6 November 2019.
16. Zong, Z.; Hu, G.; Jiang, Y.; Zou, L. Prediction of Short-Term Extreme Response of Floating Offshore Wind Turbine Under Storm Condition. In Proceedings of the ASME 2020 39th International Conference on Ocean, Offshore and Arctic Engineering, Virtual, 3–7 August 2020.
17. Chen, M.; Xiao, P.; Zhou, H.; Li, C.B.; Zhang, X. Fully Coupled Analysis of an Integrated Floating Wind-Wave Power Generation Platform in Operational Sea-States. *Front. Energy Res.* **2022**, *10*, 931057. [[CrossRef](#)]
18. Chandrasekaran, S.; Uddin, S.A. Postulated Failure Analyses of a Spread-Moored Semi-Submersible. *Innov. Infrastruct. Solut.* **2020**, *5*, 36. [[CrossRef](#)]
19. Chandrasekaran, S.; Uddin, S.A.; Wahab, M. Dynamic Analysis of Semi-Submersible Under the Postulated Failure of Restraining System with Buoy. *Int. J. Steel Struct.* **2020**, *21*, 118–131. [[CrossRef](#)]
20. Zhang, L.; Shi, W.; Zeng, Y.; Michailides, C.; Zheng, S.; Li, Y. Experimental Investigation on the Hydrodynamic Effects of Heave Plates Used in Floating Offshore Wind Turbines. *Ocean Eng.* **2023**, *267*, 113103. [[CrossRef](#)]
21. Tao, L.; Dray, D. Hydrodynamic Performance of Solid and Porous Heave Plates. *Ocean Eng.* **2008**, *35*, 1006–1014. [[CrossRef](#)]
22. An, S.; Faltinsen, O.M. An Experimental and Numerical Study of Heave Added Mass and Damping of Horizontally Submerged and Perforated Rectangular Plates. *J. Fluids Struct.* **2013**, *39*, 87–101. [[CrossRef](#)]
23. Zhu, L.; Lim, H.C. Hydrodynamic Characteristics of a Separated Heave Plate Mounted at a Vertical Circular Cylinder. *Ocean Eng.* **2017**, *131*, 213–223. [[CrossRef](#)]
24. Wilson, R.V.; Carrica, P.M.; Stern, F. Unsteady RANS Method for Ship Motions With Application to Roll for a Surface Combatant. *Comput. Fluids* **2006**, *35*, 501–524. [[CrossRef](#)]
25. Robertson, A.; Jonkman, J.; Masciola, M.; Song, H. *Definition of the Semisubmersible Floating System for Phase II of OC4*; NREL Technical Report; NREL: Golden, CO, USA, 2014; p. TP-5000-60601.
26. Kalitzin, G.; Medic, G.; Iaccarino, G.; Durbin, P. Near-Wall Behavior of RANS Turbulence Models and Implications for Wall Functions. *J. Comput. Phys.* **2005**, *204*, 265–291. [[CrossRef](#)]
27. Burmester, S.; Vaz, G.; Gueydon, S.; el Moctar, O. Investigation of a Semi-Submersible Floating Wind Turbine in Surge Decay Using CFD. *Ship Technol. Res.* **2018**, *67*, 2–14. [[CrossRef](#)]
28. Tao, L.; Molin, B.; Scolan, Y.M.; Thiagarajan, K. Spacing Effects on Hydrodynamics of Heave Plates on Offshore Structures. *J. Fluids Struct.* **2007**, *23*, 1119–1136. [[CrossRef](#)]
29. Jiang, Y.; Hu, G.; Zong, Z.; Zou, L.; Jin, G. Influence of an Integral Heave Plate on the Dynamic Response of Floating Offshore Wind Turbine Under Operational and Storm Conditions. *Energies* **2020**, *13*, 6122. [[CrossRef](#)]
30. Yu, C.; Hu, Z.; Wang, S. Investigation of Heave Response of the Deepwater Octagonal FDP SO Using Various Heave Plate Configurations. *J. Mar. Sci. Appl.* **2017**, *16*, 446–457. [[CrossRef](#)]
31. Thiagarajan, K.P.; Troesch, A.W. Effects of Appendages and Small Currents on the Hydrodynamic Heave Damping of TLP Columns. *J. Offshore Mech. Arct. Eng.* **1998**, *120*, 37–42. [[CrossRef](#)]

Disclaimer/Publisher's Note: The statements, opinions and data contained in all publications are solely those of the individual author(s) and contributor(s) and not of MDPI and/or the editor(s). MDPI and/or the editor(s) disclaim responsibility for any injury to people or property resulting from any ideas, methods, instructions or products referred to in the content.